ROYAL SOCIETY
OF CHEMISTRY

PAPER

Check for updates

Understanding phase evolution of ferroelectric Hf$_{0.5}$Zr$_{0.5}$O$_2$ thin films with Al$_2$O$_3$ and Y$_2$O$_3$ inserted layers†

Jonghoon Shin,[a] Haengha Seo,[a] Kun Hee Ye,[ab] Yoon Ho Jang,[a] Dae Seon Kwon,[a] Junil Lim,[a] Tae Kyun Kim,[a] Heewon Paik,[a] Haewon Song,[a] Ha Ni Kim,[a] Seungyong Byun,[a] Seong Jae Shin,[a] Kyung Do Kim,[a] Yong Bin Lee,[a] In Soo Lee,[a] Jung-Hae Choi [iD][b] and Cheol Seong Hwang [iD] *[a]

This study investigates the insertion traits of the Al$_2$O$_3$ and Y$_2$O$_3$ insertion layers (ILs) and their effects on the phase evolution and electrical characteristics of polycrystalline Hf$_{0.5}$Zr$_{0.5}$O$_2$ (HZO) thin films grown by atomic layer deposition (ALD). The Al$_2$O$_3$ and Y$_2$O$_3$ ILs are located at the middle position along the HZO film. The thick Al$_2$O$_3$ IL, above 2–3 ALD cycles, forms a continuous layer, physically separating the upper and lower regions of the film. Conversely, the thin Al$_2$O$_3$ IL, below 2–3 ALD cycles, and all the Y$_2$O$_3$ IL diffuse into the nearby HZO layers, making a single Al- or Y-doped HZO layer. The most crucial finding is that the diffused trivalent Al and Y ions substitute the tetravalent Hf and Zr ions, creating oxygen vacancies for charge neutrality and changing the phase evolutions. The substituted Al and Y suppress the monoclinic phase and enhance the tetragonal phase. Ultimately, the study suggests a new perspective on doped HfO$_2$-based thin films, highlighting the crucial role of substitutional diffusion of dopants and charge neutrality in determining the formation of the tetragonal phase.

1. Introduction

Research on the ferroelectric (FE) properties of HfO$_2$-based films has been accelerated since it was first reported in 2011.[1–7] Various dopants such as Si, Al, Zr, Y, Gd, Sr, and La are known to induce FE properties,[1,8–14] and the Hf$_{1−x}$Zr$_x$O$_2$ solid solution system has garnered particular attention due to its lower processing temperature and diverse material properties depending on the Hf : Zr composition ratio.[11,15–25] The changing characteristics of Hf$_{1−x}$Zr$_x$O$_2$ thin films, such as dielectric (DE), FE, and field-induced ferroelectric (FFE) properties, are due to the formation of the monoclinic phase (m-phase, space group: $P2_1/c$), orthorhombic phase (o-phase, space group: $Pca2_1$), and tetragonal phase (t-phase, space group: $P4_2/nmc$), respectively. Although the m-phase is the thermodynamically stable crystalline phase at 1 atm and room temperature, metastable o- and t-phases were achieved depending on doping concentrations, film thickness, and annealing

conditions during fabrication.[11,15–25] Many studies reported the phase transitions experimentally and theoretically, considering thermodynamic parameters and kinetic transition barriers. It is currently understood that grain size, oxygen vacancy, interfacial/surface energy, and strain/stress could complexly affect the free energy of each phase. In addition, the kinetic energy barriers between the t-, o-, and m-phases also play a crucial role in determining the final phase fraction after cooling from the crystallization annealing.[15–20,26–36]

Doping with aliovalent ions affects all these aspects for forming various phases. The influence of dopant size and valency on the FE characteristics of polycrystalline, doped-HfO$_2$ films deposited by atomic layer deposition (ALD) is widely recognized. It has been experimentally demonstrated that dopants larger (Y, Gd, La, Sr) and smaller (Si, Al) than Hf ions induce the cubic phase (c-phase, space group: $Pm\bar{3}m$) and t-phase, respectively, with the appearance of FFE properties limited to the smaller dopants.[7,37,38] However, the precise origins underlying these observed behaviors remain subject to ongoing investigation.

When the films are grown by ALD, all the material, including the dopants, are deposited layer-by-layer, which sometimes interferes adversely with homogeneous doping. The behavior of the inserted dopant layers at the sub-nm scale depends on how the ALD cycles are arranged. For example, when six cycles

[a] Department of Materials Science and Engineering, and Inter-University Semiconductor Research Center, Seoul National University, Seoul, 08826, Republic of Korea. E-mail: cheolsh@snu.ac.kr

[b] Center for Electronic Materials, Korea Institute of Science and Technology, Seoul, 02792, Republic of Korea

This journal is © The Royal Society of Chemistry 2024

J. Mater. Chem. C, 2024, **12**, 5035–5046 | **5035**

of doping layers are inserted into 60 cycles of HfO$_2$, the doping layers could be inserted in a way that one per ten, two per twenty, three per thirty, or six total in the middle of the HfO$_2$ cycles. These dopant layer insertion methods may induce different doping profiles.

Seo *et al.* systematically compared the effects of the Al$_2$O$_3$ and Y$_2$O$_3$ insertion layer (IL) on the crystallization and lattice strain of the ZrO$_2$ film when inserted in the middle of it.[39] Both dopants were trivalent ions, with the Al^{3+} and Y^{3+} ions smaller and larger than the Zr^{4+} ion. The Al$_2$O$_3$ ILs with thicknesses below ∼0.3 nm diffused into the ZrO$_2$ films without causing the ZrO$_2$ film separation but imposing the in-plane tensile stress. In contrast, thicker ILs above ∼0.3 nm formed a continuous layer, effectively separating the upper and lower parts of the ZrO$_2$ films. However, the Y$_2$O$_3$ diffused into the ZrO$_2$ films without inducing film separation, regardless of the thickness, leading to the generation of in-plane compressive stress.[39] They also reported the growth strain variation of the undoped ZrO$_2$ films depending on their thickness. The films were grown on metallic TiN substrates. The observed shifts in grazing-angle incidence X-ray diffraction (GIXRD) positions of the t(111) peaks revealed that the thinner ZrO$_2$ films were subjected to strong in-plane compressive stress. However, an increase in thickness resulted in the neutralization of the in-plane compressive stress and a gradual transition to the in-plane tensile stress, which was attributed to the Volmer–Weber type growth.[39] Generally, the ALD deposition of fluorite-structured polycrystalline thin films on metallic or Si substrates is known to exhibit the Volmer–Weber type growth.[17,40–42]

In the ZrO$_2$ thin film, the t-phase is primarily stabilized without undergoing phase transitions. Therefore, the observed GIXRD t(111) peak shifts in the previous study were readily attributed to the strain induced by diffused ions or growth strain of the ZrO$_2$ film.[39] However, when the IL is inserted into the Hf$_{1-x}$Zr$_x$O$_2$ system, the phase evolutions between t-, o-, and m-phases may be influenced. The GIXRD peak most commonly analyzed in the Hf$_{1-x}$Zr$_x$O$_2$ system is the o(111)/t(011) peak, which appears near ∼30.6°. However, accurately identifying this peak is challenging due to the overlap of the o(111) and t(011) peaks at similar positions. Moreover, strain resulting from diffused ions and phase changes can affect the shifts in GIXRD peaks for the doped Hf$_{1-x}$Zr$_x$O$_2$ system, further complicating the interpretation.[13,15,17,21,28]

In this study, the Al$_2$O$_3$ and Y$_2$O$_3$ ILs are inserted into the middle of Hf$_{0.5}$Zr$_{0.5}$O$_2$ (HZO) films to investigate the influence of dopants on phase changes. Trivalent dopants with ionic sizes smaller (Al) and larger (Y) than the Hf and Zr ions, respectively, were selected to ascertain whether ionic size plays a crucial role in the phase formation, as previously reported.[7,37,38] The findings of this study revealed that the substitutional diffusion of trivalent ions is the critical factor governing the stabilization of the t-phase and the suppression of the m-phase in polycrystalline, doped-HZO films deposited by ALD.

In this study, the films were denoted as Alp(q nm) or Yp(q nm), with the p referring to the ALD cycle number of ILs and the q nm referring to the total thickness of the HZO layers.

For example, Al1(9 nm) and Y1(9 nm) indicate the 9 nm-thick HZO film with one cycle of Al$_2$O$_3$ and one cycle of Y$_2$O$_3$, respectively. HZO samples without any ILs were labeled as q nm HZO.

In the subsequent sections, the undoped 5 nm HZO, 10 nm HZO, and 19.5 nm HZO are evaluated first for comparison with the Al$_2$O$_3$/Y$_2$O$_3$-inserted HZO films in the subsequent sections. Then, the Alp(10 nm), Alp(19.5 nm), Yp(10 nm), and Yp(19.5 nm) samples are evaluated to investigate the ILs' insertion traits and their effects on the HZO phase changes.

2. Results and discussion

This study examines the alterations in the peak positions, full width at half maximum (FWHM), and peak intensities of the GIXRD patterns to identify the variations in the strain and phases. The strain estimation from the 2θ position shifts of GIXRD peaks requires additional explanation. For the given X-ray incidence angle relative to the film surface, 0.5° in this case, the crystallographic plane with a diffraction angle of 2θ is inclined from the film surface direction by $\theta - 0.5°$ (or its normal vector is inclined from the surface normal direction by the same angle). Therefore, the precise strain calculation requires the conversion of the strain estimated from the achieved 2θ value to the surface normal direction, which Mohr's circle analysis could perform.[17] However, when the 2θ value is ∼30 and 35° in this work, the difference between the angle the two crystallographic planes are inclined from the film surface direction ($\theta - 0.5°$) is minute, so the relative increase (or decrease) in the 2θ positions represents the decrease (or increase) in d-spacing induced by the in-plane tensile (or compressive) stress in the thin films. Therefore, the strain evolution by the film growth or doping effect could be deduced by observing changes in peak positions.

The relative increase (or decrease) of FWHM with changing HZO thickness or IL cycles reflects the grain size reduction (or increment). Similarly, changes in peak intensity indicate variations in grain size, with increased (or decreased) intensities signifying increased (or decreased) grain size.

The commonly observed GIXRD peak for the HZO system is the o(111)/t(011) peak. It has been extensively reported that the o(111) and t(011) peaks overlap at $2\theta \approx 30.6°$, and an increase in the t-phase relative to the o-phase leads to an increase in the peak position.[13,15,17,21,28] Consequently, the position of the o(111)/t(011) peaks are influenced by both strain evolutions and phase fraction changes in HZO films, posing a challenge in distinguishing between these two factors.

Alternatively, the diffraction peaks near $2\theta \approx 35.5°$ could be examined to address these challenges. These peaks have been relatively less scrutinized in the past, although it has been indicated that o(200), o(020), o(002), and t(110) peaks may be overlapped.[13] Park *et al.* reported the *in situ* XRD experiments of Al-, Gd-, Sr-, and Si-doped HfO$_2$ thin films with changing temperatures.[43] The diffraction peaks near ∼30.6° shifted to lower positions with increasing temperature after crystallization,

5036 | *J. Mater. Chem. C*, 2024, **12**, 5035–5046

This journal is © The Royal Society of Chemistry 2024

which implies the increased o-phase portion relative to the t-phase. In contrast, the diffraction peaks near $\sim 35.5°$ (denoted as o(002) peaks for simplicity) showed negligible shifts with increasing temperature despite the transitions between the o- and t-phases.[43] Hence, the minimal peak shift of o(002) peaks indicates that the phase portion changes between the o- and t-phases do not affect the shift of these peaks, but only the strain evolutions can do, in contrast to the o(111)/t(011) peaks. Therefore, the subsequent sections scrutinize the contrasting changes in o(002) and o(111)/t(011) peak positions to identify the strain and phase evolution effects separately. In addition, the aspect ratio (AR) and unit cell volume changes are observed to confirm the deduced phase changes, as discussed later.

2.1 Undoped HZO film

Fig. S1(a) and (b) in the ESI,† show the background subtracted GIXRD and the Gaussian deconvoluted curves of the 5, 10, and 19.5 nm HZO samples after post-metallization annealing (PMA). Fig. 1(a) shows the changes in the 2θ positions of the deconvoluted o(002) and o(111)/t(011) peaks with changing thickness, respectively. Both o(002) and o(111)/t(011) peaks of the 10 nm HZO showed significant shifts to higher 2θ positions compared to the 5 nm HZO, suggesting that the thinner film was under the in-plane compressive stress. In contrast, the 19.5 nm HZO did not display a noticeable shift compared to the 10 nm HZO, which is consistent with the Volmer–Weber type growth mechanism.[40–42] In the early island growth stage, traction between the island and the substrate is imposed, resulting in compressive intrinsic stress. With further growth, the islands coalesce to form grain boundaries and tensile stress is

generated due to the reduction in surface energy caused by the grain boundary zipping.[40–42] The increase in tensile stress cancels out the compressive stress from the previous stage. It continues until the increase in strain energy is balanced with the decrease in surface energy and reaches a saturated state.[40,41] Hence, the relatively lower 2θ positions of the 5 nm HZO were attributed to the residual in-plane compressive stress from the island growth stage. In contrast, the higher saturated 2θ positions of the 10 and 19.5 nm HZO were attributed to the release of the compressive stress and development of in-plane tensile stress, coinciding with the previously reported growth strain behavior in ZrO_2 with changing thickness.[39]

Fig. 1(b) shows the changes in the FWHM values of the deconvoluted o(002) and o(111)/t(011) peaks, respectively. The FWHM of both o(002) and o(111)/t(011) peaks showed a gradual decrease due to the grain size increase with the increasing thickness. Fig. 1(c) shows the changes in the peak intensities of the deconvoluted o(002) and o(111)/t(011) peaks, respectively. Both peaks showed a gradual intensity increase attributed to the enhanced grain growth with increasing HZO thickness.

Fig. 1(d) shows the relative m-phase fraction changes with increasing thickness. The m-phase GIXRD peak areal fraction was calculated using $(I_{m(-111)} + I_{m(111)})/(I_{m(-111)} + I_{m(111)} + I_{o(111)/t(011)})$, where $I_{x(hkl)}$ denotes the areal intensity of the $x(hkl)$ peak in the GIXRD pattern.[11,35] Previous studies indicated the desirable rapid thermal annealing (RTA) temperature for the crystallization of HZO films to enhance their FE properties and minimize the m-phase formation 450–500 °C.[2,15,29,34] This study employed a slightly higher RTA annealing temperature of 525 °C to investigate the effect of
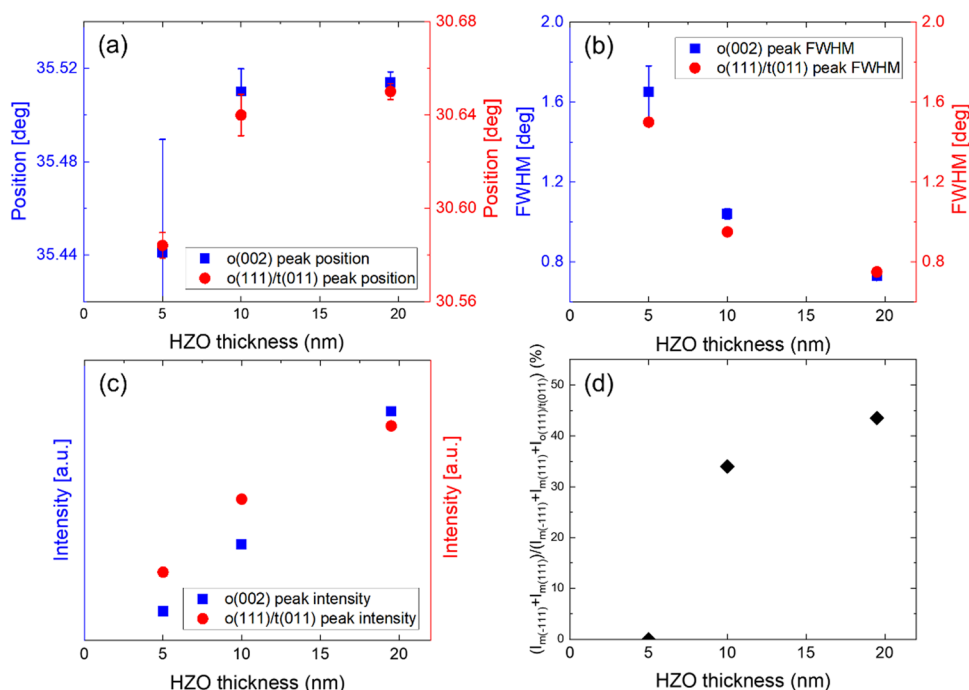

Fig. 1 The (a) peak positions, (b) FWHM, and (c) peak intensities of the o(002) and o(111)/t(011) peaks, and the (d) m-phase areal ratio for the undoped 5, 10, and 19.5 nm HZO films. Error bars are included for the peak positions and FWHM values from the standard deviation of the Gaussian fitting.

the ILs on the m-phase formation (or suppression) more clearly in the subsequent sections. The 5 nm HZO did not exhibit any m-phase, whereas the 10 nm HZO and 19.5 nm HZO showed a significant m-phase areal fraction increase up to $\sim$34% and $\sim$44% due to the enhanced grain growth in the thicker films.[2,28,29,34,35] The peak positions, FWHM, peak intensities, and m-phase areal fractions of the undoped HZO films observed in this section serve as a reference in the subsequent sections for the doped films.

2.2 Al$_2$O$_3$-inserted HZO film

Fig. S2(a) and (b) in the ESI,† show GIXRD patterns of the as-deposited Alp(10 nm) and Alp(19.5 nm) samples, respectively. The Al$_2$O$_3$ IL insertion did not significantly affect the amorphous-like structure of the Alp(10 nm) films. However, it slightly suppressed the as-deposited crystallization for the thicker Alp(19.5 nm) HZO films, indicating a potential reduction of the m-phase after PMA.[35,44]

Fig. S3(a) and (b) in the ESI,† show the background subtracted GIXRD patterns and the Gaussian deconvoluted curves of the 5, 10 nm HZO, and Alp(10 nm) samples after PMA. Fig. 2(a) shows the changes in the 2θ positions of the deconvoluted o(002) and o(111)/t(011) peaks for the Alp(10 nm) samples with changing Al$_2$O$_3$ IL cycles, respectively, where $p = 0$ case corresponds to the 10 nm HZO film. In Fig. 2(a), the blue and red dashed lines indicate the positions of the 5 nm HZO film for the o(002) and o(111)/t(011) peaks, respectively. In both peak cases, the changes displayed differences for the Al1, 2(10 nm) and Al3, 4, 6, and 8(10 nm) samples. Both o(002) and o(111)/t(011) peak positions of the Al1, 2(10 nm) samples were shifted to higher 2θ positions compared to the 10 nm HZO. According to Seo et al., the shift of the peaks to a higher position at low Al$_2$O$_3$ ALD cycles was attributed to Al^{3+} ions

(ionic radius: 53.5 pm) substitutionally diffusing into the Zr^{4+} sites (ionic radius: 72 pm) without interrupting the continuous growth, causing in-plane tensile stress to the film.[39] Due to the similar radius of the Hf^{4+} ions (ionic radius: 72 pm) to the Zr^{4+} ions, a similar insertion trait is expected for the HZO films. In contrast, the positions of the Al3, 4, 6, and 8(10 nm) films show a value similar to the 10 nm HZO ($2\theta \sim 35.52°$ for o(002) and $\sim$30.64° for o(111)/t(011)). According to Seo et al., higher ALD cycles of Al$_2$O$_3$ formed a continuous layer, physically dividing the ZrO$_2$ into two separate parts without diffusing into the Zr^{4+} sites and did not impose doping-induced stress.[39] Therefore, the similar peak positions suggested that the thicker Al$_2$O$_3$ divided the 10 nm HZO films into two $\sim$5 nm parts.

To confirm these Al$_2$O$_3$ IL insertion traits for the HZO films, spherical-aberration-corrected transmission electron microscopy (Cs-TEM) images of Al1(9 nm) and Al5(9 nm) after PMA are presented in Fig. 3(a) and (b), respectively. The Al1(9 nm) exhibited a well-crystallized single layer, suggesting that the extremely thin IL ($\sim$0.1 nm) did not disrupt the continuous growth and diffused into the nearby HZO films. In contrast, the Al5 IL ($\sim$0.5 nm) separated the HZO film into the upper and lower layers. These results were further supported by the inverse fast Fourier transform (iFFT) images in the inset figures, as well as the magnified images in Fig. 3(c) and (d). These TEM results corroborate the GIXRD results in Fig. 2(a). Therefore, the subsequent parts explain the Al1, 2(10 nm) and Al3, 4, 6, and 8(10 nm) samples separately.

When comparing the position shifts of the Al1, 2(10 nm) samples in Fig. 2(a), it is noteworthy that the o(111)/t(011) peaks showed larger shifts compared to the o(002) peaks. Considering the minimal difference in inclination angles between the normal direction of the o(111)/t(011) and o(002) planes to the film surface normal direction, the $\varepsilon_{\text{o(111)/t(011)}}$
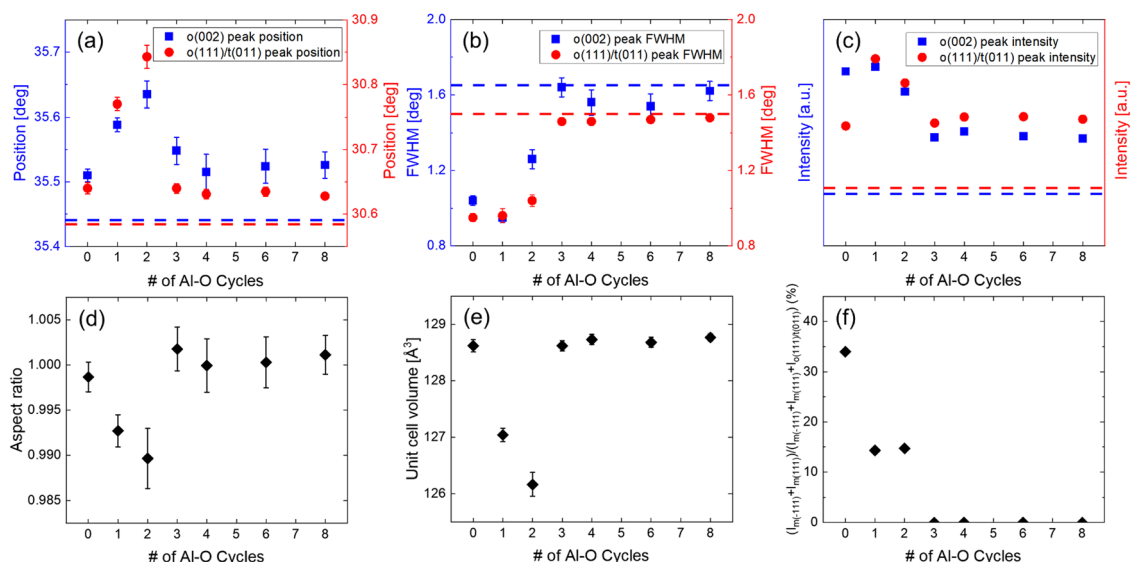

Fig. 2 The (a) peak positions, (b) FWHM, and (c) peak intensities of the o(002) and o(111)/t(011) peaks, and the (d) aspect ratio, (e) unit cell volume, and (f) m-phase areal ratio for the Alp(10 nm) films. The 5 nm HZO is also added for comparison with blue (o(002) peak) and red (o(111)/t(011) peak) dashed lines. Error bars are included for the peak positions and FWHM values from the standard deviation of the Gaussian fitting. Error bars of the aspect ratio and unit cell volume are estimated from the error of the peak positions of the o(002) and o(111)/t(011) peaks.
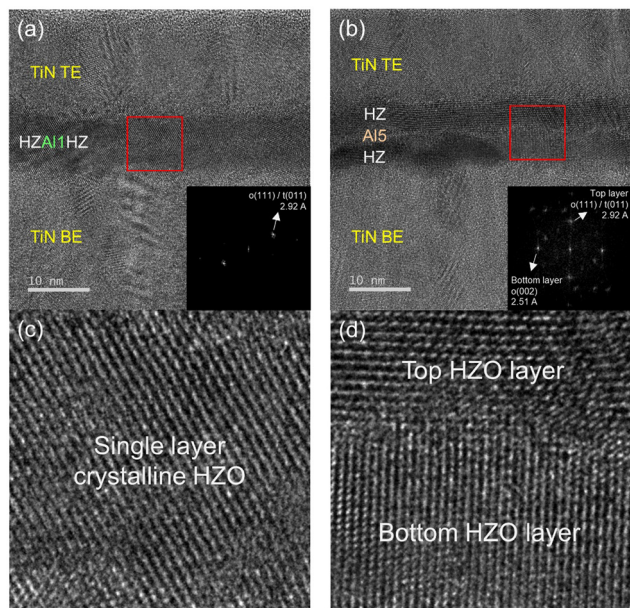
5038 | *J. Mater. Chem. C*, 2024, **12**, 5035–5046

This journal is © The Royal Society of Chemistry 2024

Fig. 3 The Cs-TEM images of the (a) Al1(9 nm) and (b) Al5(9 nm) films, with the iFFT images of the regions indicated by the red squares. The magnified images of the regions indicated by the red squares are shown in (c) Al1(9 nm) and (d) Al5(9 nm), respectively.

strain induced by Al diffusion on the o(111)/t(011) planes should be similar to the $\varepsilon_{o(002)}$ strain on the o(002) planes. Therefore, the observed differences in peak shifts should not be as pronounced as observed, suggesting factors other than in-plane tensile stress from Al diffusion may have additionally contributed to the observed o(111)/t(011) peak shifts. It can be assumed that the o(002) peaks were shifted by only the in-plane tensile stress from the diffused Al ions. In contrast, the o(111)/t(011) peaks may have been additionally shifted by an increased t(011)/(t(011) + o(111)) phase portion, as further discussed later.

When observing the peak positions of the Al3, 4, 6, and 8(10 nm) samples, it is noticeable that they have higher 2θ values than those of the 5 nm HZO, although the thicker ILs separate the 10 nm thick HZO film into two ~5 nm HZO parts. As explained in the previous section, the bottom ~5 nm HZO part must be influenced by the in-plane compressive stress from the nucleation.[40–42] However, the top parts were grown on the amorphous Al_2O_3 layer, and consequently, the residual in-plane compressive stress could be released, shifting the peak positions to slightly higher 2θ values than the 5 nm HZO film. This shift must be more pronounced as the GIXRD is more sensitive to the top part of the film.

Fig. 2(b) shows the changes in the FWHM of the o(002) and o(111)/t(011) peaks for the Alp(10 nm) samples with changing Al_2O_3 IL cycles, respectively. The FWHM values of the Al1, 2(10 nm) for the o(002) (~0.95–1.26) and o(111)/t(011) (~0.96–1.04) peaks were similar to those of the 10 nm HZO (o(002): ~1.04/o(111)/t(011): ~0.95) since the interposed Al_2O_3 did not separate the HZO layer or disrupt the grain growth. In contrast, the FWHM values of the Al3, 4, 6, and 8(10 nm) for the o(002) (~1.54–1.64) and o(111)/t(011) (~1.46–1.48) peaks are similar to those of the 5 nm HZO (o(002): ~1.65/o(111)/t(011): ~1.50), also corroborating the layer separation effect of the thick Al_2O_3 layer.

Fig. 2(c) shows the changes in the peak intensities of the o(002) and o(111)/t(011) peaks for the Alp(10 nm) samples with changing Al_2O_3 IL cycles, respectively. The o(002) and o(111)/t(011) peak intensities of the Al3, 4, 6, and 8 (10 nm) were approximately twice that of the 5 nm HZO, confirming the presence of two separated ~5 nm HZO layers. The o(002) peak intensities of the Al1, 2(10 nm) samples are comparable to those of the 10 nm HZO since the thin IL does not separate the 10 nm HZO film.

To confirm the speculations from peak positions shifts that the diffused Al enhanced the t(011)/(t(011) + o(111)) phase portion, the AR and unit cell volume changes were examined, as shown in Fig. 2(d) and (e), respectively. Park *et al.* suggested that the AR and unit cell volume are lower in the t-phase rich film than in the o-phase rich case for the polycrystalline HfO_2-based thin films.[13] It was extensively reported that the proportion of the o- and t-phases could be evaluated by observing the two factors.[13,43] The AR and unit cell volume change could be calculated from the peak positions in Fig. 2(a). The lattice parameters were calculated from interplanar spacing d_{111} and d_{002} of o(111)/t(011) and o(002) peaks under the assumption that the differences of two shorter axis latter parameters were negligible. The AR (o-phase: $2a/(b + c)$, t-phase: c/a) and the unit cell volume ($a \times b \times c$) were calculated from the lattice parameters.[13,43]

For the Al1, 2(10 nm) samples, the AR and unit cell volume values were lower than the 10 nm HZO, indicating the enhanced portion of the t-phase relative to the o-phase. The decreased percentage of the AR values was ~0.6–0.9%, smaller than the theoretical AR differences between the t- and o-phases (~2%), indicating the co-existence of the o-phase in these films. However, the decreased percentage of the unit cell volume was ~1.2–1.9%, comparable to the theoretical unit cell volume differences between the t- and o-phases (~1.5–2%).[43] This finding is because the Al-doping generally decreases the unit cell volume due to its smaller ionic radius than Hf^{4+} and Zr^{4+} ions.[13] The AR and unit cell volume values of the Al3, 4, 6, and 8(10 nm) samples showed minimal changes since the division of the HZO films did not significantly affect the relative portion changes between the o- and t-phases as the diffused Al cases. The AR and unit cell volume changes correlated well with phase changes deduced from comparatively observing the o(002) and o(111)/t(011) peak shifts, confirming its validity.

Fig. 2(f) shows the relative m-phase fraction changes for the Alp(10 nm) samples with changing Al_2O_3 IL cycles. The Al3, 4, 6, and 8(10 nm) exhibited complete suppression of the m-phase due to the interrupted grain growth.[2,28,29,34,35] This m-phase areal fraction was equal to the undoped 5 nm HZO, as the films were separated into two ~5 nm-thick HZO layers.

The Al1, 2(10 nm) showed a markedly decreased m-phase areal fraction (~15%) compared to the 10 nm HZO (~34%), despite the Al_2O_3 not interrupting grain growth. The decreased

This journal is © The Royal Society of Chemistry 2024

J. Mater. Chem. C, 2024, **12**, 5035–5046 | **5039**

m-phase must lead to the increase of the o- or t-phase portions in the films. Through a comparative analysis of the o(002) and o(111)/t(011) peak shifts, along with calculations of AR and unit cell volume of the Al1, 2(10 nm) films, it was concluded that there was an increased t/(o + t) phase portion with Al diffusion. Therefore, the dominant effect of Al diffusion appears to change the m-phase to the t-phase. The electrical characteristics tests were conducted to validate this hypothesis.

Fig. 4(a) shows the polarization–electric field (P–E) curves of the Alp(10 nm) samples in the pristine state (dotted curve for the 10 nm HZO for comparison). Fig. 4(b) shows the $2P_r$ and the $+E_c - (-E_c)$ changes of the P–E curves displayed in Fig. 4(a). The 5 nm HZO film was too electrically leaky to achieve reliable P–E curves. The P–E data displayed distinct differences for the diffused Al_2O_3 and continuous Al_2O_3 samples, which is consistent with the GIXRD data. The Al1, 2(10 nm) samples showed antiferroelectric (AFE)-like P–E curves with lower $2P_r$ ($\sim$22.8–24 µC cm^{-2}) and $+E_c - (-E_c)$ values ($\sim$1.9–1.95 MV cm^{-1}) compared to the 10 nm HZO, confirming that the Al diffusion decreased the m-phase and increased the t-phase. The curves did not show a complete AFE curve, as typically observed in the Zr-rich $Hf_{1-x}Zr_xO_2$ ($0.7 \leq x \leq 1$), due to the co-existence of the o-phase in these films.[4,21,45] On the other hand, the Al3, 4, 6, and 8(10 nm) samples exhibited FE-like P–E curves with a slightly slanted shape. This behavior could be attributed to the marginal increase in the t/(o + t) phase portion caused by the reduced thickness of two separated $\sim$5 nm HZO layers, attributed to the lower surface energy of the t-phase than the o-phase.[15,34,35] Nevertheless, the $2P_r$ values ($\sim$34.7–36.5 µC cm^{-2}) were higher than the Al1, 2(10 nm) samples, confirming a substantially more dominant o-phase portion in these films. These samples displayed higher $+E_c - (-E_c)$ values ($\sim$2.75–3.02 MV cm^{-1}) than the 10 nm HZO, as the continuous Al_2O_3 layer acted as a series resistor during the FE switching.[28,46] The gradual increase of the $+E_c - (-E_c)$ values with increasing Al cycles (3–8 cycles) was attributed to the increasing tunneling resistance of the IL film with increasing its thickness.[28,46]

Similar GIXRD and P–E analyses were performed for 10, 19.5 nm HZO, and Alp(19.5 nm) samples to validate these trends further. Fig. S4(a) and (b) in the ESI,† show the background subtracted GIXRD patterns and the Gaussian deconvoluted curves of the 10, 19.5 nm HZO, and Alp(19.5 nm) samples after PMA. Fig. S5(a)–(f) in the ESI,† show the peak position, FWHM, peak intensity, AR, unit cell volume, and m-phase areal ratio. The changes in these parameters for the Alp(19.5 nm) films indicated similar insertion effects and phase changes with the Alp(10 nm) samples. The thinner Al_2O_3 diffused into the nearby HZO, which reduced the m-phase and enhanced the t-phase. The thicker Al_2O_3 divided the HZO into two $\sim$10 nm parts.

However, there were several differences from the thinner film cases. For the Al3, 4, 6, and 8(10 nm) cases, both the o(002) and o(111)/t(011) peak positions showed noticeably higher shifts compared to those of the 5 nm HZO. However, the o(002) and o(111)/t(011) peak positions of the Al2, 3, 4, 6, and 8(19.5 nm) samples show negligible shifts compared to those of the 10 nm HZO. This difference is because the lower $\sim$10 nm HZO part of the Al2, 3, 4, 6, and 8(19.5 nm) samples were not influenced by the growth strain effects at this thickness, as explained in the previous section.

Also, Al2, 3, 4, 6, and 8(19.5 nm) samples showed retained m-phases with a peak areal fraction of $\sim$29–33%, in contrast to the Al3, 4, 6, and 8(10 nm) samples, where the m-phase was not observed. This difference was due to the thicker films being separated into two $\sim$10 nm-thick HZO layers, showing a similar m-phase areal fraction to the undoped 10 nm HZO ($\sim$34%). Additionally, the AR and unit cell volume of Al1(19.5 nm), with the diffused Al_2O_3, decreased compared to the 19.5 nm HZO by $\sim$0.3% and $\sim$0.5%, showing smaller decreases compared to the Al1, 2(10 nm) cases in Fig. 2(d) and (e), indicating that the t-phase enhancement effects of the diffused Al_2O_3 for the Al1(19.5 nm) were less pronounced than the thinner Al1, 2(10 nm) films.

Fig. S6(a) and (b) in the ESI,† show the P–E curves and the changes in the $2P_r$ and $+E_c - (-E_c)$ values of the Alp(19.5 nm)
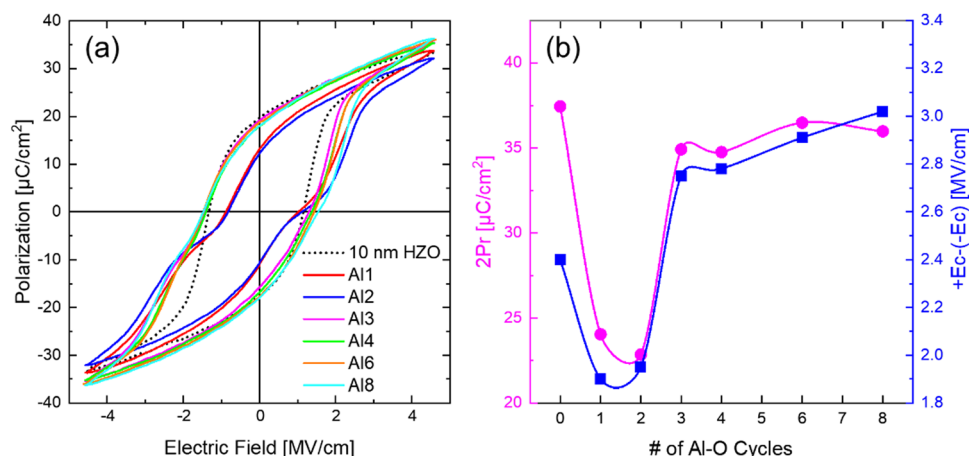

Fig. 4 (a) P–E curves and the (b) changes in the $2P_r$ and $+E_c - (-E_c)$ values of the 10 nm HZO with insertion of changing ALD cycles of Alp(10 nm) in the middle of films.

5040 | *J. Mater. Chem. C*, 2024, **12**, 5035–5046

This journal is © The Royal Society of Chemistry 2024

samples in the pristine state. The Al2, 3, 4, 6, and 8(19.5 nm) samples displayed increased $2P_r$ values due to the layer separation reducing the m-phase and enhancing the o/(m + o + t) phase portion in the films. The Al1(19.5 nm) sample with the diffused Al_2O_3 showed reduced $2P_r$ and $+E_c - (-E_c)$ values compared to the undoped 19.5 nm HZO film, confirming that the diffused Al reduced the m-phase and enhanced the t-phase. However, the impact of diffused Al_2O_3 on the changes in electrical characteristics was less pronounced when inserted in the center of 19.5 nm HZO compared to 10 nm HZO. These results are consistent with AR and unit cell volume changes. It is plausible that the m-phase suppression and t-phase enhancement were more pronounced in the regions of the HZO film closer to the diffused Al_2O_3. The ratio of the HZO film affected by the t-phase enhancement may be smaller in the case of 19.5 nm HZO compared to 10 nm HZO, considering that the total thickness of HZO is approximately twice as large in the former case.

Fig. 5(a)–(c) show the X-ray photoelectron spectroscopy (XPS) spectra of Hf 4f, Zr 3d, and Al 2p, respectively, of the Al1, 3, and 5(7.8 nm) samples. The Hf 4f and Zr 3d spectra of the Al1(7.8 nm) sample shifted to lower binding energy positions than the 7.8 nm HZO. The deconvolution of these spectra revealed the formation of substantial oxygen-deficient phases (HfO_{2-x}, ZrO_{2-x}).[25,47] These phases originated from the substitutional diffusion of Al^{3+} ions into the Hf^{4+} and Zr^{4+} ion sites, inducing oxygen vacancies to maintain charge neutrality.[48] In contrast, the Hf 4f and Zr 3d spectra of Al3, 5(7.8 nm) samples showed minimal change in their binding energy values, and the deconvolution revealed the formation of minuscule oxygen-deficient phases. The Al 2p spectra in Fig. 5(c) showed that the binding energy of Al1(7.8 nm) (74.05 eV) was higher compared to those of Al3, 5(7.8 nm) (73.96 eV, 73.97 eV), suggesting that the Al oxidation number increased from the nominal 3+ in the Al_2O_3 for the diffused IL. These findings
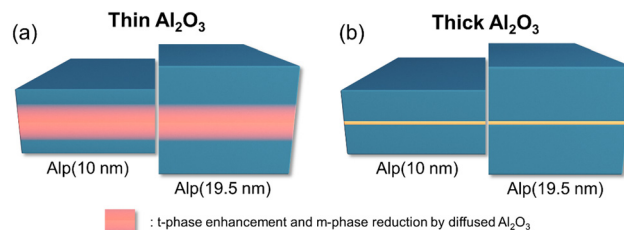

Fig. 6 Schematic diagrams of the effects of Al_2O_3 ILs on the 10 nm and 19.5 nm HZO thin films. (a) The thin Al_2O_3 diffused into the HZO, inducing in-plane tensile stress. The diffusion enhanced the t-phase and reduced the m-phase for the nearby regions. The thicker 19.5 nm HZO film was less influenced by the diffusion. (b) The thick Al_2O_3 formed a continuous layer, dividing the film into two parts.

agree well with previous observations that the thick Al_2O_3 IL did not diffuse into the HZO but formed a separate layer. In contrast, the thin Al_2O_3 IL substitutionally diffused into the HZO. Previous studies indicated that creating a slightly oxygen-deficient condition for the HfO_2-based films can suppress the m-phase formation and promote the t-phase.[7,30,31,49,50] The diffused Al_2O_3 generated oxygen vacancies, effectively reducing the m-phase and enhancing the t-phase formation.

Fig. 6(a) and (b) summarize the effects of Al_2O_3 ILs when inserted in the middle of 10 nm and 19.5 nm HZO films. The thinner Al_2O_3 substitutionally diffused into the HZO without impeding the continuous growth and introduced in-plane tensile stress to the film. The Al_2O_3 layer reduced the m-phase and enhanced the t-phase due to the oxygen vacancies generated by the substitutional diffusion of Al^{3+} ions into the Hf^{4+} and Zr^{4+} sites in the 10 nm HZO film. The thicker HZO film was less influenced by the Al-doping effect, where only the region near the Al_2O_3 IL was affected.

In contrast, the thick Al_2O_3 layer remained a continuous layer. It separated the upper and lower regions of the HZO film,
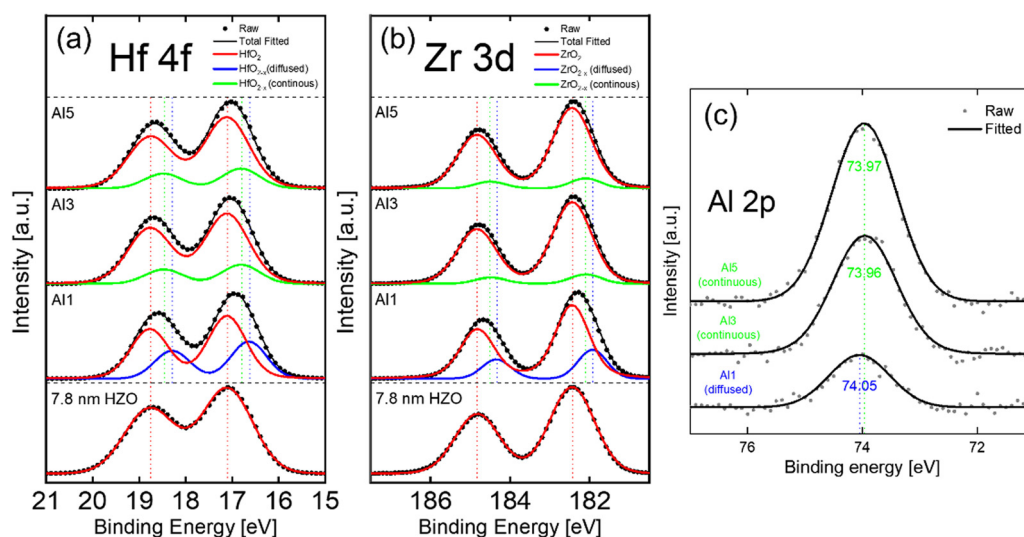

Fig. 5 The baseline subtracted XPS (a) Hf 4f, (b) Zr 3d, and (c) Al 2p spectra of the Al1, 3, and 5(7.8 nm). The Hf 4f and Zr 3d spectra of the sample without interlayer are also compared.

This journal is © The Royal Society of Chemistry 2024

J. Mater. Chem. C, 2024, **12**, 5035–5046 | **5041**

resulting in a significant reduction of the m-phase through suppressed grain growth. The formation of either the t-phase or the o-phase was favored depending on the physical thickness of the individual divided layers. Fig. S7(a)–(c) in the ESI,† shows the defect formation energy of the substitutional configurations of Al in the HZO. The calculation results coincide with the previous work, confirming the thickness-dependent substitutional diffusion characteristics of the Al$_2$O$_3$ ILs for the HZO system.[39]

2.3 Y$_2$O$_3$-inserted HZO film

Fig. S8(a) and (b) in the ESI,† show GIXRD of the as-deposited Yp(10 nm) and Yp(19.5 nm) samples, respectively. The Y$_2$O$_3$ IL insertion slightly enhanced the as-deposited crystallization of the HZO films, indicating a possible increase of the m-phase after PMA from conventional understanding.[35,44] However, this study revealed a different trend, as discussed later.

Fig. S9(a) and (b) in the ESI,† show the background subtracted GIXRD patterns and the Gaussian deconvoluted curves of the 10 nm HZO and Yp(10 nm) samples after PMA. Fig. 7(a) shows the changes in the 2θ positions of the deconvoluted o(002) and o(111)/t(011) peaks for the Yp(10 nm) samples with changing Y$_2$O$_3$ IL cycles, respectively. The o(002) peaks of Y1, 2, 4, 6, and 8(10 nm) were shifted monotonically to lower 2θ positions with increasing p. This peak position shift indicates the involvement of the in-plane compressive stress as the Y^{3+} ions (ionic radius: 90 pm) substitutionally diffuse into the Hf^{4+} and Zr^{4+} sites (ionic radius: 72 pm) without interrupting the continuous growth.[39]

To check this Y$_2$O$_3$ IL insertion effect in HZO films, a Cs-TEM image of Y4(9 nm) after PMA is presented in Fig. 8(a), which exhibited a well-crystallized single layer. This observation was further supported by the iFFT image in the inset Fig and the magnified image in Fig. 8(b). Hence, these results
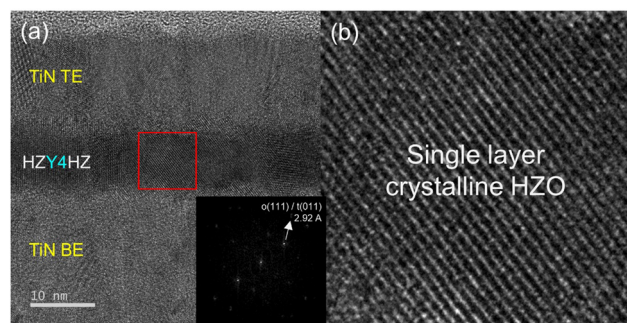

Fig. 8 The (a) Cs-TEM image of the Y4(9 nm) film, with the iFFT image of the region indicated by the red square. The magnified image of the region indicated by the red square is shown in (b).

suggested that the Y$_2$O$_3$ ILs substitutionally diffused into the nearby HZO films without interrupting the continuous growth.

In contrast, the o(111)/t(011) peak position shows a markedly different trend, as shown in Fig. 7(a). Up to two cycles of Y$_2$O$_3$ ALD, it increases and then decreases from four cycles, following the trend of the o(002) peaks. Following the discussion in the previous section, such a temporal increase in the peak position indicates the enhanced t(011)/(t(011) + o(111)) phase portion in the films. Again, such a trend cannot be detected from the o(002) peak, as only the strain evolution governs its position.

Fig. 7(b) shows the changes in the FWHM, and Fig. 7(c) shows the changes in the peak intensities of the deconvoluted o(002) and o(111)/t(011) peaks for the Yp(10 nm) samples with changing Y$_2$O$_3$ IL cycles, respectively. In the lower Y$_2$O$_3$ cycles, the FWHM of both o(002) and o(111)/t(011) peaks exhibited a gradual decrease compared to the 10 nm HZO film, while the peak intensities showed a gradual increase. These changes suggested that the diffused Y$_2$O$_3$ enhanced the grain growth
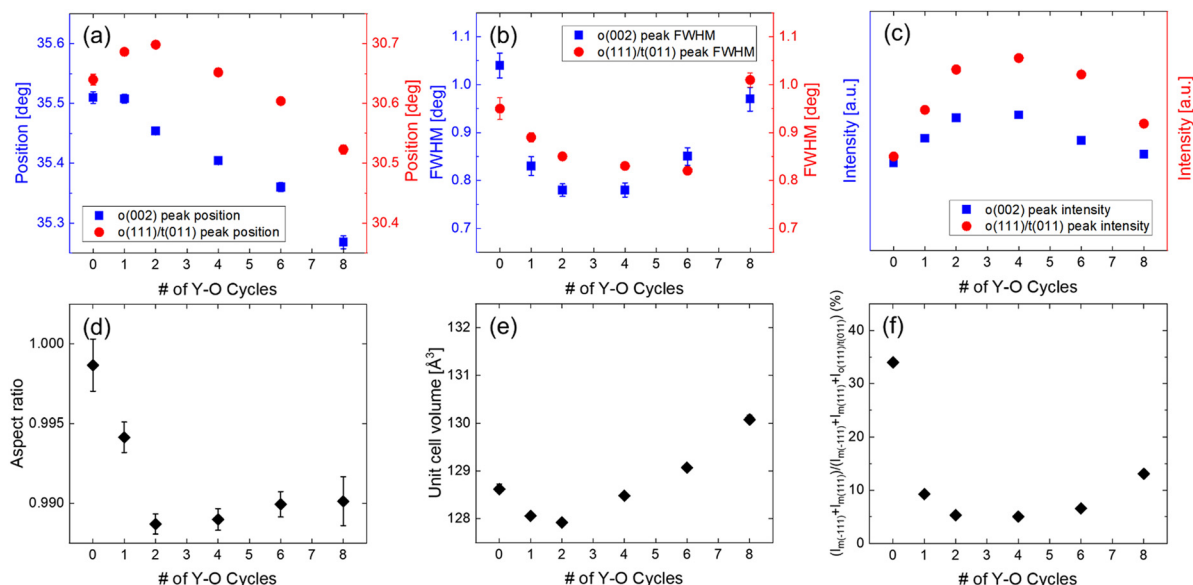

Fig. 7 The (a) peak positions, (b) FWHM, and (c) peak intensities of the o(002) and o(111)/t(011) peaks, and the (d) aspect ratio, (e) unit cell volume, and (f) m-phase areal ratio for the Yp(10 nm) films. Error bars are included for the peak positions and FWHM values from the standard deviation of the Gaussian fitting. Error bars of the aspect ratio and unit cell volume are estimated from the error of the peak positions of the o(002) and o(111)/t(011) peaks.

5042 | *J. Mater. Chem. C*, 2024, **12**, 5035–5046

This journal is © The Royal Society of Chemistry 2024

at lower cycles. For higher Y_2O_3 cycles, the FWHM of both peaks showed increased values, accompanied by a decrease in peak intensities, suggesting that the HZO films developed into a mosaic structure.

To further confirm that the diffused Y enhanced the $t/(o + t)$ phase portion, the AR and unit cell volume changes were presented in Fig. 7(d) and (e), respectively. The AR values of $Yp(10\ nm)$ samples decreased with increasing p at lower p, confirming that the Y diffusion enhanced the $t/(o + t)$ phase portion.[13,43] Interestingly, the AR values saturated at $p \geq 2$. This saturation may be due to the limited impact of diffused Y_2O_3 on the phase changes within the nearby regions of the HZO, with regions farther away from the ILs remaining unaffected even with the increased p. The decreased percentage of the AR values was ~ 0.5–1%, smaller than the theoretical AR differences between the t- and o-phases due to the copresence of the o-phase.[43]

The unit cell volume of $Yp(10\ nm)$ samples decreased up to $p = 2$ and increased for Y4, 6, and 8(10 nm). This change could be attributed to the combined influence of the relative portion changes between the o- and t-phases and the ionic radius of diffused Y^{3+}.[13] For $p < 2$, the t-phase formation effect dominates, but for $p > 2$, the larger Y^{3+} radius effect dominates.

Fig. 7(f) shows the relative m-phase fraction changes for the $Yp(10\ nm)$ samples with changing Y_2O_3 IL cycles. The $Yp(10\ nm)$ samples exhibited a remarkably decreased m-phase areal fraction of ~ 5–13% compared to the 10 nm HZO ($\sim 34\%$), despite the Y_2O_3 ILs not interrupting the continuous growth. This decrease indicated that the added portion of the o- and t-phases in the films increased compared to the undoped film. The observation of peak positions, AR, and unit cell volume of the $Yp(10\ nm)$ samples indicated the increased $t/(o + t)$ phase portion with Y diffusion. Hence, the diffused Y_2O_3 reduces the m-phase and enhances the t-phase, as in the diffused Al_2O_3 cases. The following electrical characteristic tests confirmed this hypothesis.

Fig. 9 shows the P–E curves of the $Yp(10\ nm)$ samples in the pristine state (dotted curve for the 10 nm HZO for comparison). They showed AFE-like P–E curves, confirming the m-phase reduction and the t-phase enhancement through Y diffusion. Similar to the Al1, 2(10 nm) cases, these films did not exhibit a complete AFE curve due to the copresence of the o-phase.[4,21,45] The Y1, 2, 4, and 6(10 nm) samples exhibited similar $2P_r$ values (~ 18.2–$19.4\ \mu C\ cm^{-2}$), indicating a comparable o-phase portion in these films. However, the Y8(10 nm) sample showed a degraded $2P_r$ value due to the formation of a mosaic structure and again increased m-phase fraction. The Y2, 4, and 6(10 nm) samples showed similar P–E curves despite the increased Y_2O_3 IL cycles. This result coincided with the AR values showing saturation at $p \geq 2$ in Fig. 7(d), even with the increased p.

Similar GIXRD and P–E analyses were performed for 19.5 nm HZO and $Yp(19.5\ nm)$ samples to validate these trends further. Fig. S10(a) and (b) in the ESI,† show the background subtracted GIXRD patterns and the Gaussian deconvoluted curves of the 19.5 nm HZO and $Yp(19.5\ nm)$ samples after PMA. Fig. S11(a)–(f) in the ESI,† show the peak position, FWHM, peak intensity, AR, unit cell volume, and m-phase areal ratio. The changes in
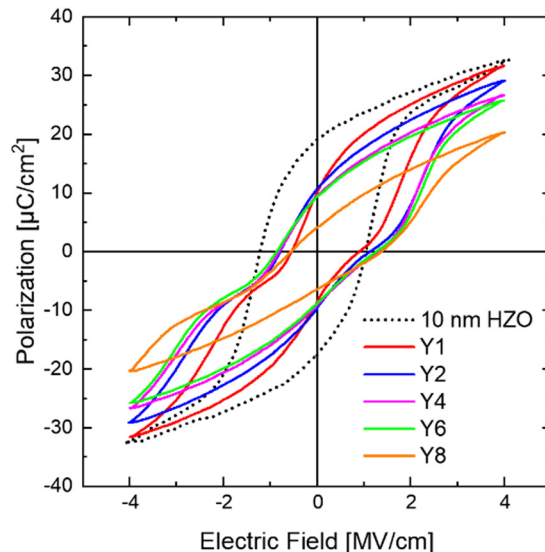

Fig. 9 P–E curves of the 10 nm HZO with insertion of changing ALD cycles of $Yp(10\ nm)$ in the middle of films.

these parameters for the $Yp(19.5\ nm)$ films indicated similar insertion effects and phase changes with the $Yp(10\ nm)$ samples. However, while the Y doping exhibited consistent effects in thicker and thinner films, its impact was less prominent in the thicker $Yp(19.5\ nm)$ films.

Fig. S12 in the ESI,† shows the P–E curves of the $Yp(19.5\ nm)$ samples in the pristine state. The P–E curves exhibited reduced $2P_r$ values compared to the 19.5 nm HZO despite the significant m-phase reduction, confirming that the Y diffusion reduced the m-phase and enhanced the t-phase. However, its impact was less prominent than the thinner $Yp(10\ nm)$ cases, aligning with the GIXRD analysis.

Fig. 10(a)–(c) show the XPS spectra of Hf 4f, Zr 3d, and Y 3d, respectively, of the Y3, 5(7.8 nm) samples. The Hf 4f and Zr 3d spectra of the Y3, 5(7.8 nm) films shifted to lower binding energy positions than the 7.8 nm HZO, and deconvolution displayed the formation of oxygen-deficient phases (HfO_{2-x}, ZrO_{2-x}), coinciding with the Al1(7.8 nm) cases in Fig. 5(a) and (b).[25,47] As for the diffused Al_2O_3 cases, the substitutional diffusion of Y^{3+} ions into the Hf^{4+} and Zr^{4+} ion sites generated oxygen vacancies, which reduced the m-phase and enhanced the t-phase.[48] The Y 3d spectra in Fig. 10(c) showed minimal binding energy changes for Y3, 5(7.8 nm) samples since the ILs were substitutionally diffused regardless of cycles.

Fig. 11 summarizes the effects of Y_2O_3 ILs when inserted in the middle of 10 nm and 19.5 nm HZO films. The Y_2O_3 IL, regardless of the number of cycles, substitutionally diffused into the HZO without hindering the continuous growth and induced stronger in-plane compressive stress to the HZO film with higher p. The diffused Y_2O_3 suppressed the m-phase and enhanced the t-phase formation due to the oxygen vacancies generated by the substitutional diffusion of Y^{3+} ions into the Hf^{4+} and Zr^{4+} sites. Fig. S7(a)–(c) in the ESI,† shows the defect formation energy of the substitutional configurations of Y in the HZO. The calculation results coincide with the previous work, thus
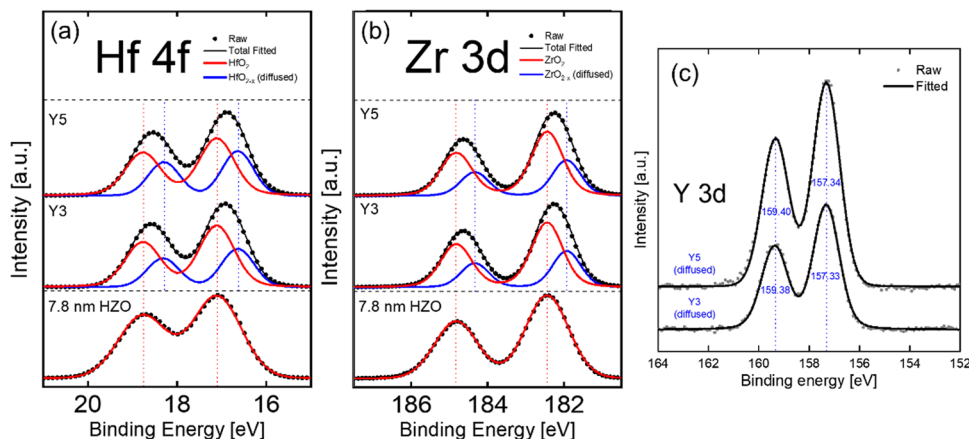
This journal is © The Royal Society of Chemistry 2024

J. Mater. Chem. C, 2024, **12**, 5035–5046 | **5043**

Fig. 10 The baseline subtracted XPS (a) Hf 4f, (b) Zr 3d, and (c) Y 3d spectra of the Y3, 5(7.8 nm). The Hf 4f and Zr 3d spectra of the sample without interlayer are also compared.
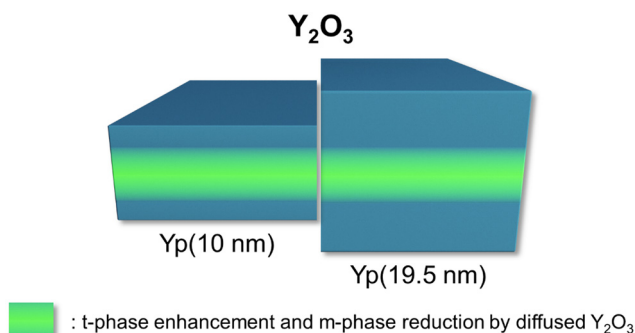

Fig. 11 Schematic diagram of the effects of Y_2O_3 ILs on the 10 nm and 19.5 nm HZO thin films. The Y_2O_3 diffused into the HZO regardless of cycles, inducing in-plane compressive stress. The diffusion enhanced the t-phase and reduced the m-phase for the nearby regions. The thicker 19.5 nm HZO film was less influenced by the diffusion.

confirming the thickness-independent substitutional diffusion characteristics of the Y_2O_3 ILs for the HZO system.[39]

Previous works have reported that dopants with ion sizes larger (Y, Gd, La, and Sr) and smaller (Si, Al) than Hf ions stabilize the c-phase and t-phase, respectively, for polycrystalline ALD HfO_2-based films. When larger dopants were doped, the t-phase was not formed, and FFE characteristics were not observed. Only the smaller dopants could stabilize the t-phase and induce FFE properties.[7]

However, the present work revealed a different conclusion. It was revealed that the Y_2O_3 IL, irrespective of p, and the thin Al_2O_3 diffused into the HZO, reducing the m-phase and enhancing the t-phase. In contrast, the thick Al_2O_3 did not diffuse into the HZO and could not form the t-phase. Consequently, this study elucidated the substitutional diffusion of Al^{3+} or Y^{3+} ions into Hf^{4+} or Zr^{4+} sites and the formation of oxygen vacancies as the critical requirement factor determining the formation of the t-phase. Even larger Y dopants could stabilize the t-phase when the trivalent ions were substitutionally diffused. The t-phase stabilization was observed previously for epitaxial Y-doped HfO_2/HZO films deposited by pulsed laser deposition (PLD). However, the t-phase stabilization was attributed to high annealing temperatures over 900 °C, converting the m-phase to the t-phase at such high temperatures, which was not the case in this study. In addition, these studies did not elucidate the substitutional diffusion of dopants as the reason for t-phase stabilization.[51–53]

These results suggest a new perspective on the phase changes of polycrystalline, doped-HfO_2-based thin films, highlighting the crucial role of substitutional diffusion of dopants and charge neutrality. These insights could guide subsequent studies on engineering the FFE properties of doped HfO_2-based thin films.

3. Experimental sections

3.1 Sample preparation

A TiN bottom electrode (BE) with a thickness of 50 nm was deposited on a thermally oxidized SiO_2(100 nm)/Si substrate *via* sputtering (ENDURA 5500, Applied Materials). HZO films and Al_2O_3 ILs were deposited *in situ* by thermal ALD at a substrate temperature of 280 °C. $Hf[N(C_2H_5)CH_3]_4$ (TEMA-Hf), $Zr[N(C_2H_5)CH_3]_4$ (TEMA-Zr), $Al(CH_3)_3$ (TMA), and ozone (concentration: 190 g m^{-3}) were used as the Hf, Zr, Al precursors, and oxygen source, respectively. Y_2O_3 ILs were deposited *ex situ* by the same thermal ALD at a substrate temperature of 250 °C. $Y(EtCp)_2(iPr-amd)$ (ARYA) and ozone (concentration: 260 g m^{-3}) were used as the Y precursor and oxygen source, respectively. EtCp and iPr-amd represent ethylcyclopentadienyl ($CH_2CH_3C_5H_5$) and isopropylamidinate ($CH(CH_3)_2CN_2CH_3$), respectively. In all cases, the ILs were positioned in the middle of the HZO film thickness. The HfO_2 and ZrO_2 growth per cycle values were ~0.14 nm per cycle, while those for Al_2O_3 and Y_2O_3 were ~0.1 nm per cycle and ~0.15 nm per cycle, respectively. The HZO films were deposited with different total numbers of HfO_2 and ZrO_2 ALD cycles, with most films being grown by 72 cycles (~10 nm) or 140 cycles (~19.5 nm). However, several films were prepared using 64 cycles (~9 nm) or 56 cycles (~7.8 nm). In all cases, the ALD cycle numbers for HfO_2 and ZrO_2 were the same to achieve a Hf:Zr composition ratio of 5:5.

5044 | *J. Mater. Chem. C*, 2024, **12**, 5035–5046

This journal is © The Royal Society of Chemistry 2024

3.2 Physical and electrical characterization

The physical thicknesses of each layer were determined using spectroscopic ellipsometry (SE; M-2000, J. A. Woollam), while the areal density ($\mu g\ cm^{-2}$) and the cation composition were analyzed using X-ray fluorescence spectroscopy (XRF; Quant'X, Thermo SCIENTIFIC). Metal shadow masks (area: $\sim 90\,000\ \mu m^2$) were used to deposit circular TiN (20 nm) top electrode (TE) *via* radio-frequency (RF) reactive sputtering (SRN 120, Sorona) at 500 W. The electrode areas were accurately measured with an optical microscope. After the TE deposition, PMA was performed at 525 °C for 30 s under an N_2 ambient condition to crystallize the films.

The *P–E* characteristics were obtained by applying a bipolar triangular pulse at a frequency of 1 kHz with a ferroelectric tester (TF Analyzer 2000, Aixacct Systems). The $2P_r$ values were obtained by subtracting the negative *y*-intercept of the *P–E* curve from the positive *y*-intercept. The film crystal structure and crystallization behavior were analyzed *via* GIXRD (X'pert Pro, PANalytical, angle of incidence = 0.5°) and Cs-TEM (JEM-ARM200F, JEOL). XPS (Axis Supra, Kratos) analysis was performed to determine the chemical bonding state of Al_2O_3 and Y_2O_3 ILs with HZO films. The binding energy of the XPS spectra was calibrated using the adventitious C signal (284.5 eV).

4. Conclusions

In conclusion, this study systematically investigated the insertion mechanism of the Al_2O_3 and Y_2O_3 ILs and their effects on the structural and electrical properties of HZO film when inserted into the middle of films. It was revealed that the behavior of Al_2O_3 insertion varied depending on the number of Al_2O_3 IL cycles. The thin Al_2O_3 IL (1–2 cycles) diffused into the HZO films without interrupting continuous growth, which caused in-plane tensile stress to the films. In contrast, the thick Al_2O_3 IL (≥ 2–3 cycles) formed a continuous layer, physically dividing the HZO film into two discontinuous parts. The Y_2O_3 IL, regardless of the number of cycles, diffused into the HZO film, inducing in-plane compressive stress and enhancing grain growth. The most crucial finding of this work is that the substitutional diffusion of Al^{3+} and Y^{3+} ions into Hf^{4+} and Zr^{4+} ion sites generated oxygen vacancies for charge neutrality, forming oxygen-deficient phases near the diffused ILs, which reduced the monoclinic phase and enhanced the formation of the tetragonal phase. Unlike the previous understanding, the larger Y dopant could also induce the tetragonal phase when diffused into the HZO films. Hence, the substitutional diffusion of dopants was unveiled as the critical factor governing the tetragonal phase formation.

The doping behavior of Al_2O_3 and Y_2O_3 ILs in the HZO system coincided with those reported by Seo *et al.* for the ZrO_2 system.[39] However, the two systems differed fundamentally because only the tetragonal phase was stabilized in the ZrO_2 system. In contrast, the impurity type and quantity affected the phase changes in the HZO system. The changes in o- and t-phase portions were identified by comparatively observing the o(002) and o(111)/t(011) peak shifts and further confirmed by examining the AR and unit cell volume changes.

Author contributions

J. Shin designed and performed the experiments and wrote the manuscript. H. Seo assisted with the experiment design and data interpretations. K. H. Ye conducted the density functional theory calculations. Y. H. Jang helped with the figure design. D. S. Kwon, J. Lim, T. K. Kim, H. Paik, H. Song, S. J. Shin, and K. D. Kim helped review the manuscript. H. N. Kim, S. Y. Byun, Y. B. Lee, and I. S. Lee assisted with the ALD deposition and device fabrication. J.-H. Choi supervised the density functional theory calculations. C. S. Hwang supervised the whole research and manuscript preparation.

Conflicts of interest

The authors declare they have no conflict of interest.

Acknowledgements

Notes and references

1 T. Böscke, J. Müller, D. Bräuhaus, U. Schröder and U. Böttger, *Appl. Phys. Lett.*, 2011, **99**, 102903.

2 M. H. Park, Y. H. Lee, H. J. Kim, Y. J. Kim, T. Moon, K. D. Kim, J. Mueller, A. Kersch, U. Schroeder and T. Mikolajick, *Adv. Mater.*, 2015, **27**, 1811–1831.

3 M. H. Park, Y. H. Lee, T. Mikolajick, U. Schroeder and C. S. Hwang, *MRS Commun.*, 2018, **8**, 795–808.

4 M. H. Park and C. S. Hwang, *Rep. Prog. Phys.*, 2019, **82**, 124502.

5 U. Schroeder, C. S. Hwang and H. Funakubo, *Ferroelectricity in doped hafnium oxide: materials, properties and devices*, Woodhead Publishing, 2019.

6 M. H. Park, D. H. Lee, K. Yang, J.-Y. Park, G. T. Yu, H. W. Park, M. Materano, T. Mittmann, P. D. Lomenzo and T. Mikolajick, *J. Mater. Chem. C*, 2020, **8**, 10526–10550.

7 U. Schroeder, M. H. Park, T. Mikolajick and C. S. Hwang, *Nat. Rev. Mater.*, 2022, **7**, 653–669.

8 S. Mueller, C. Adelmann, A. Singh, S. Van Elshocht, U. Schroeder and T. Mikolajick, *ECS J. Solid State Sci. Technol.*, 2012, **1**, N123.

9 S. Mueller, J. Mueller, A. Singh, S. Riedel, J. Sundqvist, U. Schroeder and T. Mikolajick, *Adv. Funct. Mater.*, 2012, **22**, 2412–2417.

10 J. Müller, T. Böscke, S. Müller, E. Yurchuk, P. Polakowski, J. Paul, D. Martin, T. Schenk, K. Khullar and A. Kersch, *presented at 2013 IEEE International Electron Devices Meeting*, 2013.

This journal is © The Royal Society of Chemistry 2024

J. Mater. Chem. C, 2024, **12**, 5035–5046 | **5045**

11 J. Muller, T. S. Boscke, U. Schroder, S. Mueller, D. Brauhaus, U. Bottger, L. Frey and T. Mikolajick, *Nano Lett.*, 2012, **12**, 4318–4323.

12 J. Müller, U. Schröder, T. Böscke, I. Müller, U. Böttger, L. Wilde, J. Sundqvist, M. Lemberger, P. Kücher and T. Mikolajick, *J. Appl. Phys.*, 2011, **110**, 114113.

13 M. H. Park, T. Schenk, C. M. Fancher, E. D. Grimley, C. Zhou, C. Richter, J. M. LeBeau, J. L. Jones, T. Mikolajick and U. Schroeder, *J. Mater. Chem. C*, 2017, **5**, 4677–4690.

14 T. Schenk, S. Mueller, U. Schroeder, R. Materlik, A. Kersch, M. Popovici, C. Adelmann, S. Van Elshocht and T. Mikolajick, *presented at 2013 Proceedings of the European Solid-State Device Research Conference (ESSDERC)*, 2013.

15 M. H. Park, H. J. Kim, Y. J. Kim, W. Lee, T. Moon and C. S. Hwang, *Appl. Phys. Lett.*, 2013, **102**, 242905.

16 M. H. Park, H. J. Kim, Y. J. Kim, W. Lee, T. Moon, K. D. Kim and C. S. Hwang, *Appl. Phys. Lett.*, 2014, **105**, 192903.

17 M. H. Park, H. J. Kim, Y. J. Kim, T. Moon and C. S. Hwang, *Appl. Phys. Lett.*, 2014, **104**, 072901.

18 T. Shimizu, T. Yokouchi, T. Shiraishi, T. Oikawa, P. S. R. Krishnan and H. Funakubo, *Jpn. J. Appl. Phys.*, 2014, **53**, 09PA04.

19 A. Chernikova, M. Kozodaev, A. Markeev, Y. Matveev, D. Negrov and O. Orlov, *Microelectron. Eng.*, 2015, **147**, 15–18.

20 R. Materlik, C. Künneth and A. Kersch, *J. Appl. Phys.*, 2015, **117**, 134109.

21 M. H. Park, H. J. Kim, Y. J. Kim, Y. H. Lee, T. Moon, K. D. Kim, S. D. Hyun and C. S. Hwang, *Appl. Phys. Lett.*, 2015, **107**, 192907.

22 M. H. Park, H. J. Kim, Y. J. Kim, T. Moon, K. D. Kim and C. S. Hwang, *Adv. Energy Mater.*, 2014, **4**, 1400610.

23 M. H. Park, H. J. Kim, Y. J. Kim, Y. H. Lee, T. Moon, K. D. Kim, S. D. Hyun, F. P. G. Fengler, U. Schroeder and C. S. Hwang, *ACS Appl. Mater. Interfaces*, 2016, **8**, 15466–15475.

24 B. Y. Kim, H. W. Park, S. D. Hyun, Y. B. Lee, S. H. Lee, M. Oh, S. K. Ryoo, I. S. Lee, S. Byun and D. Shim, *Adv. Electron. Mater.*, 2022, **8**, 2100042.

25 B. Y. Kim, I. S. Lee, H. W. Park, Y. B. Lee, S. H. Lee, M. Oh, S. K. Ryoo, S. R. Byun, K. D. Kim and J. H. Lee, *Adv. Mater. Technol.*, 2023, 2300146.

26 D. Cunningham, *Honors Scholar Thesis*, 2014, **359**.

27 S. Estandia, N. Dix, J. Gazquez, I. Fina, J. Lyu, M. F. Chisholm, J. Fontcuberta and F. Sanchez, *ACS Appl. Electron. Mater.*, 2019, **1**, 1449–1457.

28 H. J. Kim, M. H. Park, Y. J. Kim, Y. H. Lee, W. Jeon, T. Gwon, T. Moon, K. D. Kim and C. S. Hwang, *Appl. Phys. Lett.*, 2014, **105**, 192903.

29 Y. H. Lee, S. D. Hyun, H. J. Kim, J. S. Kim, C. Yoo, T. Moon, K. D. Kim, H. W. Park, Y. B. Lee and B. S. Kim, *Adv. Electron. Mater.*, 2019, **5**, 1800436.

30 T. Mittmann, T. Szyjka, H. Alex, M. C. Istrate, P. D. Lomenzo, L. Baumgarten, M. Müller, J. L. Jones, L. Pintilie and T. Mikolajick, *Phys. Status Solidi RRL*, 2021, **15**, 2100012.

31 W. Hamouda, A. Pancotti, C. Lubin, L. Tortech, C. Richter, T. Mikolajick, U. Schroeder and N. Barrett, *J. Appl. Phys.*, 2020, **127**, 064105.

32 M. H. Park, H. J. Kim, G. Lee, J. Park, Y. H. Lee, Y. J. Kim, T. Moon, K. D. Kim, S. D. Hyun and H. W. Park, *Appl. Phys. Rev.*, 2019, **6**, 041403.

33 M. H. Park, Y. H. Lee and C. S. Hwang, *Nanoscale*, 2019, **11**, 19477–19487.

34 M. H. Park, Y. H. Lee, H. J. Kim, Y. J. Kim, T. Moon, K. Do Kim, S. D. Hyun, T. Mikolajick, U. Schroeder and C. S. Hwang, *Nanoscale*, 2018, **10**, 716–725.

35 M. H. Park, Y. H. Lee, H. J. Kim, T. Schenk, W. Lee, K. Do Kim, F. P. Fengler, T. Mikolajick, U. Schroeder and C. S. Hwang, *Nanoscale*, 2017, **9**, 9973–9986.

36 M. H. Park, Y. H. Lee, T. Mikolajick, U. Schroeder and C. S. Hwang, *Adv. Electron. Mater.*, 2019, **5**, 1800522.

37 C.-K. Lee, E. Cho, H.-S. Lee, C. S. Hwang and S. Han, *Phys. Rev. B: Condens. Matter Mater. Phys.*, 2008, **78**, 012102.

38 U. Schroeder, E. Yurchuk, J. Müller, D. Martin, T. Schenk, P. Polakowski, C. Adelmann, M. I. Popovici, S. V. Kalinin and T. Mikolajick, *Jpn. J. Appl. Phys.*, 2014, **53**, 08LE02.

39 H. Seo, I. W. Yeu, D. S. Kwon, D. G. Kim, J. Lim, T. K. Kim, H. Paik, J. H. Choi and C. S. Hwang, *Adv. Electron. Mater.*, 2022, **8**, 2200099.

40 Y. Lee, H. W. Jeong, S. H. Kim, K. Yang and M. H. Park, *Mater. Sci. Semicond. Process.*, 2023, **160**, 107411.

41 J. S. Tello and A. F. Bower, *J. Mech. Phys. Solids*, 2008, **56**, 2727–2747.

42 W. Nix and B. Clemens, *J. Mater. Res.*, 1999, **14**, 3467–3473.

43 M. H. Park, C. C. Chung, T. Schenk, C. Richter, K. Opsomer, C. Detavernier, C. Adelmann, J. L. Jones, T. Mikolajick and U. Schroeder, *Adv. Electron. Mater.*, 2018, **4**, 1800091.

44 K. Do Kim, Y. H. Lee, T. Gwon, Y. J. Kim, H. J. Kim, T. Moon, S. D. Hyun, H. W. Park, M. H. Park and C. S. Hwang, *Nano Energy*, 2017, **39**, 390–399.

45 M. H. Park, H. J. Kim, Y. H. Lee, Y. J. Kim, T. Moon, K. Do Kim, S. D. Hyun and C. S. Hwang, *Nanoscale*, 2016, **8**, 13898–13907.

46 A. Q. Jiang, H. J. Lee, G. H. Kim and C. S. Hwang, *Adv. Mater.*, 2009, **21**, 2870–2875.

47 T. V. Perevalov, I. P. Prosvirin, E. A. Suprun, F. Mehmood, T. Mikolajick, U. Schroeder and V. A. Gritsenko, *J. Sci.: Adv. Mater. Dev.*, 2021, **6**, 595–600.

48 M. Pešić, F. P. G. Fengler, L. Larcher, A. Padovani, T. Schenk, E. D. Grimley, X. Sang, J. M. LeBeau, S. Slesazeck and U. Schroeder, *Adv. Funct. Mater.*, 2016, **26**, 4601–4d612.

49 M. Materano, P. D. Lomenzo, A. Kersch, M. H. Park, T. Mikolajick and U. Schroeder, *Inorg. Chem. Front.*, 2021, **8**, 2650–2672.

50 Y. H. Lee, H. J. Kim, T. Moon, K. Do Kim, S. D. Hyun, H. W. Park, Y. B. Lee, M. H. Park and C. S. Hwang, *Nanotechnology*, 2017, **28**, 305703.

51 T. Mimura, T. Shimizu, T. Kiguchi, A. Akama, T. J. Konno, Y. Katsuya, O. Sakata and H. Funakubo, *Jpn. J. Appl. Phys.*, 2019, **58**, SBBB09.

52 T. Shimizu, Y. Tashiro, T. Mimura, T. Kiguchi, T. Shiraishi, T. J. Konno, O. Sakata and H. Funakubo, *Phys. Status Solidi RRL*, 2021, **15**, 2000589.

53 T. Mimura, Y. Tashiro, T. Shimizu and H. Funakubo, *ACS Appl. Electron. Mater.*, 2023, **5**, 1600–1605.

5046 | *J. Mater. Chem. C*, 2024, **12**, 5035–5046

This journal is © The Royal Society of Chemistry 2024